#### **PAPER • OPEN ACCESS**

## Solving inverse scattering problems via reducedorder model embedding procedures

To cite this article: Jörn Zimmerling et al 2024 Inverse Problems 40 025002

View the article online for updates and enhancements.

## You may also like

- On extension of the data driven ROM inverse scattering framework to partially nonreciprocal arrays
  V Druskin, S Moskow and M Zaslavsky
- Estimation of the Born data in inverse scattering of layered media
  Zekui Jia, Maokun Li, Fan Yang et al.
- An Adaptive Reduced-Order-Modeling Approach for Simulating Real-Time
  Performances of Li-Ion Battery Systems Meng Guo, Xinfang Jin and Ralph E. White



Inverse Problems 40 (2024) 025002 (25pp)

## Solving inverse scattering problems via reduced-order model embedding procedures

## Jörn Zimmerling<sup>1</sup>, Vladimir Druskin<sup>2</sup>, Murthy Guddati<sup>3</sup>, Elena Cherkaev<sup>4</sup> and Rob Remis<sup>5,\*</sup>

- <sup>1</sup> Scientific Computing Division, Department of Information Technology, Uppsala University, Lägerhyddvägen 1, 751 05 Uppsala, Sweden
- Worcester Polytechnic Institute, 100 Institute Road, Stratton Hall, Worcester, MA 01609, United States of America
- <sup>3</sup> North Carolina State University, 2501 Stinson Drive, Mann Hall 419, Raleigh, NC 27695, United States of America
- <sup>4</sup> Department of Mathematics, College of Science, University of Utah, 155 South 1400 East, JWB 233, Salt Lake City, UT 84112, United States of America
- <sup>5</sup> Terahertz Sensing Group, Delft University of Technology, Mekelweg 4, 2628 CD Delft, The Netherlands

E-mail: R.F.Remis@tudelft.nl

Received 14 June 2023; revised 13 October 2023 Accepted for publication 12 December 2023 Published 22 December 2023



#### Abstract

We present a reduced-order model (ROM) methodology for inverse scattering problems in which the ROMs are data-driven, i.e. they are constructed directly from data gathered by sensors. Moreover, the entries of the ROM contain localised information about the coefficients of the wave equation. We solve the inverse problem by embedding the ROM in physical space. Such an approach is also followed in the theory of 'optimal grids,' where the ROMs are interpreted as two-point finite-difference discretisations of an underlying set of equations of a first-order continuous system on this special grid. Here, we extend this line of work to wave equations and introduce a new embedding technique, which we call Krein embedding, since it is inspired by Krein's seminal work on vibrations of a string. In this embedding approach, an adaptive grid and a set of medium parameters can be directly extracted from a ROM and we show that several limitations of optimal grid embeddings can be avoided. Furthermore,

Original Content from this work may be used under the terms of the Creative Commons Attribution 4.0 licence. Any further distribution of this work must maintain attribution to the author(s) and the title of the work, journal citation and DOI.

Author to whom any correspondence should be addressed.

we show how Krein embedding is connected to classical optimal grid embedding and that convergence results for optimal grids can be extended to this novel embedding approach. Finally, we also briefly discuss Krein embedding for open domains, that is, semi-infinite domains that extend to infinity in one direction.

Keywords: inverse scattering, reduced-order models, embedding, optimal grids

#### 1. Introduction

In this paper we discuss so-called reduced-order model (ROM) embedding procedures to solve inverse scattering problems. In such a procedure, data-driven ROMs are constructed from spectral impedance data collected at one end of a bounded interval of interest. Subsequently, a ROM is interpreted as a two-point finite-difference discretisation of an underlying set of first-order continuous wave equations. We refer to this step as embedding of the ROM in physical space and it is this embedding procedure that allows us to determine the medium parameters on the spatial interval of interest. Applications of the inverse problems considered in this paper can be found in radar, geophysical exploration in crystalline bedrock, ground penetrating radar, and any other field where one-dimensional imaging is relevant [4]. The characterisation of transmission lines (wave speed reconstruction along coax cables, printed circuit boards, etc) also belongs to this problem class [5, 11].

Different solution procedures have been developed for the scattering problems considered in this paper (see the different Newton/optimisation methods in the overview paper [18], for example). The proposed embedding techniques presented here, however, have several advantages over methods based on optimisation. First, the embedding procedures are direct (noniterative) methods, which is generally computationally advantageous compared to optimisation. Second, for the case of a bounded interval with Dirichlet boundaries, convergence of the reconstructed medium to the true medium is guaranteed, whereas optimisation may converge to a local minimum. Third, the methods are computationally optimal in extracting the same number of parameters as there are data points and, finally, the considered embedding approaches need no regularisation. Embedding as discussed in this paper also has connections with discrete Gelfand–Levitan theory via the Lanczos algorithm. These connections are addressed in [3, 15].

Two embedding procedures are discussed in this paper. The first, called *optimal grid embedding*, is based on the theory of (optimal) truncated spectral measure grids [3]. We consider the recovery of a velocity profile from the first poles and residues of the impedance function, the so-called truncated spectral measure. An implementation of this procedure in terms of travel time coordinates is presented in [4]. Here, we take this optimal grid procedure as a starting point and present optimal grid embedding in terms of spatial coordinates instead of travel time coordinates.

However, a drawback of optimal grid embedding is that it requires training for a known medium, data, and boundary conditions. More specifically, to retrieve the spatially varying medium parameters on a certain bounded interval of interest, we first have to determine an optimal grid for a homogeneous reference medium. Having this trained reference grid available, the position dependent medium parameters can be determined on the interval of interest. Moreover, the length of this interval must be included in training as well, but this information is not always available. In radar imaging, for example, the distance to the surface may not be

known exactly and for problems on semi-infinite domains, the step sizes quickly become very large [10].

The use of a reference grid is avoided in the second embedding procedure presented in this paper, which is a new procedure that we call *Krein embedding*, since it is inspired by Krein's seminal work on vibrations of a string [12, 13]. Furthermore, the length of the interval of interest is not required either. We also show how Krein embedding is related to optimal grid embedding and that convergence results presented in [3] for optimal truncated spectral measure grids essentially carry over to the Krein embedding approach.

Since a trained reference grid and the length of a reconstruction interval are not required for Krein embedding, such an embedding approach may be applied to scattering problems on semi-infinite domains as well, that is, domains that extend to infinity in one direction. Furthermore, scattering problems on semi-infinite domains characterised by continuous spectral measures can equivalently be described by scattering poles that correspond to passive dissipative systems [17]. Our approach is then to construct ROMs that can be interpreted as a finite-difference discretisation of a dissipative first-order system. We call this *Krein–Nudelman embedding*, since the case of a dissipative boundary condition was discussed by Krein and Nudelman in [13].

However, for problems on semi-infinite domains a uniqueness problem arises, since the method embeds an impedance function provided in pole-residue form, which cannot distinguish between a lossy bounded domain and a lossless open domain. In the latter case, the spectrum is not a point spectrum but is represented as such. Nevertheless, if we apply a Krein–Nudelman embedding approach to such a problem, we find that the medium profile is actually recovered up until the last reflector, where Krein–Nudelman embedding places an absorbing effective medium to match the (complex) point spectrum of the impedance function. A numerical example will be presented that illustrates this phenomenon and the uniqueness problem is discussed further in appendix A.

The remainder of this paper is organised as follows. In section 2 we discuss the construction of the ROMs from spectral data and the optimal grid and Krein embedding procedures that may be used to retrieve the medium parameters on a bounded interval. Subsequently, these two procedures are discussed in detail in sections 3 and 4, while in section 5 a number of numerical examples are presented that illustrate the performance of both embedding procedures. Finally, Krein-Nudelman embedding on a semi-infinite domain is briefly discussed in section 6 and the conclusions can be found in section 7.

### 2. Embedding of ROMs

We are interested in reconstructing the wave speed c in the wave equation from boundary measurements. We formulate the problem in the temporal Laplace domain with complex Laplace frequency  $s \in \mathbb{C}$  and reflecting boundary conditions. Specifically, on the bounded interval [0,L] of interest, the governing Laplace-domain equation is given by

$$\frac{d^2 u(x,s)}{dx^2} - s^2 \frac{1}{c^2(x)} u(x,s) = 0, \quad \frac{du}{dx} \Big|_{x=0} = -s, \quad \text{and} \quad u|_{x=L} = 0.$$
 (1)

This problem is equivalent to the equation for a vibrating string studied by Kac and Krein [12] if  $c^{-2}(x)$  is replaced by the mass density of a string. The above equation also follows from the telegrapher equations for a transmission line that is short-circuited at the far-end of the line and a unit current is fed into the near-end of the line. In this case, c(x) represents the wave speed along the transmission line.

For a given wave speed profile, equation (1) essentially represents a regular Sturm–Liouville problem. We are also interested in the corresponding singular case in which equation (1) is considered on the semi-infinite interval  $[0,\infty)$  with the boundary condition for u at x=L replaced by the condition that  $|u(x)| \to 0$  as  $x \to \infty$  for Re(s) > 0.

In both the regular and singular case, the associated inverse problem is to recover c(x) from measurements of the impedance function f(s) = u(0,s) for s on some curve in the complex plane. The spectral inverse problem that we consider in this paper consists of the reconstruction of c(x) from poles and residues of the impedance function f(s). In particular, we assume to have access to the first n complex-conjugate pairs of poles  $\lambda_j$  and residues  $y_j$  of the function f(s). In an application, this spectral information is not readily available from measurements of f(s). However, it can be retrieved from the measured impedance function f(s) using the vectorfit algorithm [8]. In the numerical experiment section, we illustrate this procedure.

Assuming that we have n complex-conjugate pole-residue pairs available, we can construct the ROM

$$f^{\text{ROM}}(s) = \sum_{j=1}^{n} \frac{y_j}{s + \lambda_j} + \frac{\bar{y}_j}{s + \bar{\lambda}_j},\tag{2}$$

where the overbar denotes complex conjugation. We look for ROMs of this form, since we consider spectral problems in which spectral impedance data is provided in pole-residue form (not pole-zero form). Furthermore, to satisfy the Schwarz reflection principle (since the coefficients in the differential equations are real and time-domain measurements are real-valued as well), the spectrum comes in conjugate pairs of poles and residues. For a regular Sturm–Liouville problem the residues  $y_j$  are real and positive and the  $\lambda_j$  are purely imaginary. However, for the singular Sturm–Liouville case discussed later this may not be the case and we therefore include conjugation in the above spectral expansion of  $f^{\text{ROM}}(s)$ . Finally, we mention that if we introduce the diagonal matrix

$$\mathbf{\Lambda} = \operatorname{diag}\left(\lambda_1, \lambda_2, \dots, \lambda_n, \bar{\lambda}_1, \bar{\lambda}_2, \dots, \bar{\lambda}_n\right) \tag{3}$$

and the residue vector

$$\mathbf{y} = \left[\sqrt{y_1}, \sqrt{y_2}, \dots, \sqrt{y_n}, \sqrt{\bar{y}_1}, \sqrt{\bar{y}_2}, \dots, \sqrt{\bar{y}_n}\right]^T \tag{4}$$

the ROM can also be written as

$$f^{\text{ROM}}(s) = \mathbf{y}^{T} (\mathbf{\Lambda} + s\mathbf{I})^{-1} \mathbf{y}, \tag{5}$$

where **I** is the  $2n \times 2n$  identity matrix.

#### 2.1. Building a ROM from spectral data

The key idea behind optimal grid and Krein embedding is to interpret the ROM  $f^{\text{ROM}}(s)$  as the impedance function of a two-point finite-difference discretisation of an underlying set of first-order differential equations. Specifically, introducing a dual variable  $\hat{u}$  and the staggered grid shown in figure 1, the first-order finite-difference system that corresponds to equation (1) is given by

$$\frac{\hat{u}_{j+1} - \hat{u}_j}{\hat{\gamma}_{j+1}} + su_j = 0, \qquad \forall j = 0, \dots, n-1, 
\frac{u_j - u_{j-1}}{\gamma_j} + s\hat{u}_j = 0, \qquad \forall j = 1, \dots, n$$
(6)

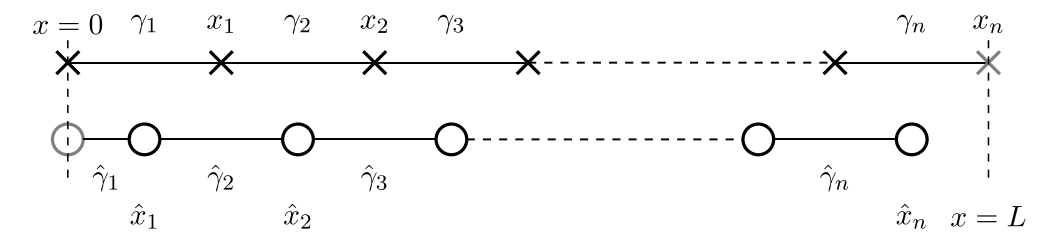


**Figure 1.** Grid used to interpret the ROM as a finite-difference discretisation of the underlying differential operator. The crosses represent primary grid nodes and the circles dual grid nodes. On the grey nodes the boundary conditions are applied.

with  $u_j = u(x_j)$  and  $\hat{u}_j = \hat{u}(\hat{x}_j)$  and where  $\gamma_j$  and  $\hat{\gamma}_j$  are the edge weights, i.e. products of the step sizes  $x_j - x_{j-1}$  and the medium parameters on the grid. The boundary conditions of the system are given by  $\hat{u}(0) = \hat{u}_0 = 1$  and  $u(L) = u_n = 0$ .

Introducing the 2*n*-by-1 vector of unknowns

$$\mathbf{u} = [u_0, \hat{u}_1, u_1, \dots, \hat{u}_{n-1}, u_{n-1}, \hat{u}_n]^T \tag{7}$$

the finite-difference system of equation (6) can be written compactly as

$$(\mathbf{T} + s\mathbf{I})\mathbf{u} = \frac{1}{\hat{\gamma}_1}\mathbf{e}_1, \tag{8}$$

where  $\mathbf{e}_1$  is the first canonical basis vector of length 2n and matrix  $\mathbf{T}$  is a tridiagonal matrix of order 2n given by

$$\mathbf{T} = \begin{pmatrix} 0 & \hat{\gamma}_1^{-1} & 0 & 0 \\ -\gamma_1^{-1} & 0 & \gamma_1^{-1} & 0 \\ \vdots & -\hat{\gamma}_2^{-1} & \ddots & \ddots \\ \vdots & & \ddots & 0 & \hat{\gamma}_n^{-1} \\ 0 & \cdots & 0 & -\gamma_n^{-1} & 0 \end{pmatrix}. \tag{9}$$

To accommodate a standard complex-symmetric Lanczos implementation further on, we prefer to work with the transpose-symmetric matrix

$$\mathbf{T}^{TS} = -i \begin{pmatrix} 0 & (\gamma_1 \hat{\gamma}_1)^{-\frac{1}{2}} & 0 & 0 \\ (\gamma_1 \hat{\gamma}_1)^{-\frac{1}{2}} & 0 & -(\gamma_1 \hat{\gamma}_2)^{-\frac{1}{2}} & 0 \\ \vdots & -(\gamma_1 \hat{\gamma}_2)^{-\frac{1}{2}} & \ddots & \ddots \\ \vdots & & \ddots & 0 & (\gamma_n \hat{\gamma}_n)^{-\frac{1}{2}} \\ 0 & \cdots & 0 & (\gamma_n \hat{\gamma}_n)^{-\frac{1}{2}} & 0 \end{pmatrix}, \tag{10}$$

instead of the tridiagonal matrix T. Matrix  $T^{TS}$  is related to matrix T by the similarity transform  $T^{TS} = STS^{-1}$ , where the similarity matrix S is given by

$$\mathbf{S} = \operatorname{diag}\left(\sqrt{\hat{\gamma}_1}, i\sqrt{\gamma_1}, \sqrt{\hat{\gamma}_2}, i\sqrt{\gamma_2}, \dots, \sqrt{\gamma_n}, i\sqrt{\gamma_n}\right). \tag{11}$$

With  $f^{\text{ROM}}(s) = u_0(s) = \mathbf{e}_1^T \mathbf{u}$  we now find that by solving the system of equation (8) for  $\mathbf{u}$  that

$$f^{\text{ROM}}(s) = \frac{1}{\hat{\gamma}_1} \mathbf{e}_1^T (\mathbf{T} + s\mathbf{I})^{-1} \mathbf{e}_1$$

$$= \frac{1}{\hat{\gamma}_1} \mathbf{e}_1^T (\mathbf{S}^{-1} \mathbf{T}^{\text{TS}} \mathbf{S} + s\mathbf{I})^{-1} \mathbf{e}_1$$

$$= \frac{1}{\hat{\gamma}_1} \mathbf{e}_1^T [\mathbf{S}^{-1} (\mathbf{T}^{\text{TS}} + s\mathbf{I}) \mathbf{S}]^{-1} \mathbf{e}_1$$

$$= \frac{1}{\hat{\gamma}_1} \mathbf{e}_1^T \mathbf{S}^{-1} (\mathbf{T}^{\text{TS}} + s\mathbf{I})^{-1} \mathbf{S} \mathbf{e}_1$$

$$= \frac{1}{\hat{\gamma}_1} \mathbf{e}_1^T (\mathbf{T}^{\text{TS}} + s\mathbf{I})^{-1} \mathbf{e}_1.$$
(12)

To extract the finite difference parameters  $\gamma_j$ ,  $\hat{\gamma}_j$  from the spectral parameters  $(\lambda_j, y_j)$  we need to transform the diagonal transfer function representation of equation (5) to the tridiagonal one of equation (12). To that end, let **Y** denote the eigenvector matrix of  $\mathbf{T}^{TS}$  such that it satisfies  $\mathbf{T}^{TS}\mathbf{Y} = \mathbf{Y}\mathbf{\Sigma}$  with  $\mathbf{Y}^T\mathbf{Y} = \mathbf{I}$  and  $\mathbf{\Sigma}$  is a diagonal matrix of order 2n with the eigenvalues of  $\mathbf{T}^{TS}$  on the diagonal. The impedance function can now be written as

$$f^{\text{ROM}}(s) = \frac{1}{\hat{\gamma}_1} \mathbf{y}_1^T (\mathbf{\Sigma} + s\mathbf{I})^{-1} \mathbf{y}_1, \tag{13}$$

where  $\mathbf{y}_1 = \mathbf{Y}^T \mathbf{e}_1$  is the vector containing the first components of all eigenvectors. Setting  $\mathbf{y}_1 = \sqrt{\hat{\gamma}_1} \mathbf{y}$  and with  $\mathbf{\Sigma} = \mathbf{\Lambda}$ , we observe that the above ROM coincides with the ROM of equation (5). Since the residue vector  $\mathbf{y}$  and the poles  $\mathbf{\Lambda}$  are known, the problem turns into an inverse eigenvalue problem in which we attempt to reconstruct the tridiagonal matrix  $\mathbf{T}^{TS}$  from the first components of its eigenvectors and its known eigenvalues. As is well known, this problem can be solved via the Lanczos algorithm. Specifically, with orthogonalization in the transpose bilinear form [14, 16], vector  $\mathbf{y}/\sqrt{\mathbf{y}^T\mathbf{y}}$  as a starting vector, and the matrix of eigenvalues  $\mathbf{\Lambda}$  as iteration matrix, the Lanczos algorithm produces the desired tridiagonal matrix. The algorithm is given in algorithm 1 and as soon as the tridiagonal matrix is obtained, the coefficients  $\gamma_j$  and  $\hat{\gamma}_j$  can be extracted using the recursive scheme shown in algorithm 2. We note that the weight  $\hat{\gamma}_1$  can be determined directly from the residues, since

$$\mathbf{y}^T \mathbf{y} = \hat{\gamma}_1^{-1} \mathbf{y}_1^T \mathbf{y}_1 = \hat{\gamma}_1^{-1}. \tag{14}$$

Finally, we also note that the algorithm explicitly computes the diagonal elements  $\alpha_j$  of matrix  $\mathbf{T}^{TS}$ , while we know that these elements vanish for lossless media. However, this very same algorithm can be used for problems on open domains or for problems involving lossy media for which the diagonal elements of matrix  $\mathbf{T}^{TS}$  may no longer vanish. Therefore, we prefer to work with this Lanczos algorithm since it accommodates all cases of interest.

**Algorithm 1.** The Lanczos algorithm for complex symmetric matrices to obtain the tridiagonal matrix  $\mathbf{T}^{TS}$  from the poles  $\boldsymbol{\Lambda}$  and residues  $\mathbf{y}$ . In this algorithm,  $\mathbf{Y}_j$  indicates the jth column of the eigenvector matrix  $\mathbf{Y}$ ,  $\alpha_j$  is the jth element on the diagonal  $(\mathbf{T}^{TS})_{j,j}$  and  $\beta_j$  the jth element on the super diagonal  $(\mathbf{T}^{TS})_{j-1,j}$  of matrix  $\mathbf{T}^{TS}$ .

```
1: procedure COMPLEX SYMMETRIC LANCZOS
                    Normalize: \mathbf{Y}_1 = \mathbf{y}/\sqrt{\mathbf{y}^T\mathbf{y}}
                    \mathbf{v}_1 = \mathbf{\Lambda} \mathbf{Y}_1
                    \alpha_1 = \mathbf{v}_1^T \mathbf{Y}_1
  4:
   5:
                    \mathbf{v}_1 = \mathbf{v}_1 - \alpha_1 \mathbf{Y}_1
                    for j=2,\ldots,2n do
   6:
                           \beta_{j} = \sqrt{\mathbf{v}_{j-1}^{T} \mathbf{v}_{j-1}}
\mathbf{if} \ \beta_{j} \neq 0 \ \mathbf{then}
\mathbf{Y}_{j} = \mathbf{v}_{j-1} / \beta_{j}
\mathbf{v}_{j} = \mathbf{\Lambda} \mathbf{Y}_{j}
\alpha_{j} = \mathbf{v}_{j}^{T} \mathbf{Y}_{j}
\mathbf{v}_{j} = \mathbf{v}_{j} - \alpha_{j} \mathbf{Y}_{j} - \beta_{j} \mathbf{Y}_{j-1}
else Brechdown
   7:
   8:
   9:
10:
11:
12:
                             else Breakdown
13:
14:
                             end if
15:
                    end for
16: end procedure
```

**Algorithm 2.** Extract the ROM parameters  $\gamma_j$  and  $\hat{\gamma}_j$  from  $\beta_j$  the super diagonal of the matrix  $\mathbf{T}^{TS}$ .

```
1: procedure EXTRACT GAMMA

2: \hat{\gamma}_1 = (\mathbf{y}_1^T \mathbf{y}_1)^{-1}

3: for j = 1, ..., n - 1 do

4: \gamma_j = -(\beta_{2j}^2 \hat{\gamma}_j)^{-1}

5: \hat{\gamma}_{j+1} = -(\beta_{2j+1}^2 \gamma_j)^{-1}

6: end for

7: \gamma_n = -(\beta_{2n}^2 \hat{\gamma}_n)^{-1}

8: end procedure
```

## 2.2. Krein and optimal grid embedding

Up to this point we constructed a ROM from the poles and residues of a boundary impedance function. The ROM can be interpreted as the impedance function of a two-point finite-difference discretization of a first-order system with primary and dual grid coefficients  $\gamma_j$  and  $\hat{\gamma}_j$ , respectively. How to interpret these coefficients depends on the dual variable  $\hat{u}$  that is introduced to obtain a first-order system of ODEs from the original second-order ODE. In particular, introducing the dual variable  $\hat{u} = -s^{-1}\partial_x u$ , the second-order system of equation (1) can be written as

$$\begin{pmatrix} s & c^2 \partial_x \\ \partial_x & s \end{pmatrix} \begin{pmatrix} u(x,s) \\ \hat{u}(x,s) \end{pmatrix} = 0, \quad u(L,s) = 0, \quad \hat{u}(0,s) = 1,$$
 (15)

and this form will lead to what we call the *Krein embedding* interpretation. On the other hand, introducing the quantities  $w = c^{-\frac{1}{2}}u$  and  $\hat{w} = c^{\frac{1}{2}}\hat{u}$  as well as the slowness coordinates (sometimes called travel time coordinates)

$$T(x) = \int_0^x \frac{1}{c(\xi)} \,\mathrm{d}\xi \tag{16}$$

we obtain the first-order system

$$\begin{pmatrix} s & c^{\frac{1}{2}} \partial_T c^{-\frac{1}{2}} \\ c^{-\frac{1}{2}} \partial_T c^{\frac{1}{2}} & s \end{pmatrix} \begin{pmatrix} w(T,s) \\ \hat{w}(T,s) \end{pmatrix} = 0, \tag{17}$$

with w(T(L),s)=0 and  $\hat{w}(0,s)=c^{\frac{1}{2}}(0)$ , and this system will leads to a standard optimal grid embedding interpretation. Note that in this latter case the impedance function is  $f(s)=u(0,s)=c^{\frac{1}{2}}(0)w(0,s)$  and that standard optimal grid embedding is formulated in terms of travel time coordinates.

In the next two sections we will give detailed descriptions of optimal grid and Krein embedding procedures for wave propagation problems. Convergence of these procedures is also briefly discussed.

## 3. Optimal grid embedding

Optimal grid embedding of ROMs was developed for the diffusion equation in [3]. In this section, we extend this embedding approach to wave propagation problems and rely on results obtained for the diffusion equation.

The main difficulty in ROM embedding is that each of the finite difference weights  $\gamma_j$  and  $\hat{\gamma}_j$  consist of a product of the unknown local medium parameter and an unknown grid step. Fortunately, for diffusion problems it has been shown that there exists a computable grid  $\{\gamma_j^0,\hat{\gamma}_j^0\}$  that is independent of the medium parameters in the limit  $n\to\infty$  (lemma 3.2 of [3]). The existence of this grid allows us to obtain the local material parameters by taking ratios of the grid steps  $\gamma_j^0,\hat{\gamma}_j^0$  and ROM parameters  $\gamma_j,\hat{\gamma}_j$  thereby reconstructing the medium. Furthermore, it can be shown the medium estimates converge pointwise in  $L^1(0,L)$  (theorem 6.1 of [3]).

As a first step towards optimal grid embedding for wave propagation, we extend the results from [3] by considering equation (17) in spatial coordinates instead of travel time coordinates. Subsequently, we take the kinematic effects into account and discuss medium parameter retrieval based on equation (17).

To avoid confusion, we call the medium parameter  $\zeta$  when considering (17) in spatial coordinates. In other words, we start by considering

$$\begin{pmatrix} s & \zeta^{\frac{1}{2}} \partial_x \zeta^{-\frac{1}{2}} \\ \zeta^{-\frac{1}{2}} \partial_x \zeta^{\frac{1}{2}} & s \end{pmatrix} \begin{pmatrix} v(x,s) \\ \hat{v}(x,s) \end{pmatrix} = 0$$
 (18)

with v(L,s)=0,  $\hat{v}(0,s)=\zeta^{\frac{1}{2}}(0)$  and transfer function  $f(s)=\zeta^{\frac{1}{2}}(0)v(0,s)$ . A staggered finite-difference grid with primary grid steps  $\delta_j$  and dual grid steps  $\hat{\delta}_j$  has the grid points

$$x_j = \sum_{i=1}^j \delta_i \quad \text{and} \quad \hat{x}_j = \sum_{i=1}^j \hat{\delta}_i \tag{19}$$

and a two-point finite-difference discretisation of the first-order system (18) gives

$$\frac{\hat{\zeta}_{j+1}^{-\frac{1}{2}}\hat{v}_{j+1} - \hat{\zeta}_{j}^{-\frac{1}{2}}\hat{v}_{j}}{\zeta_{j}^{\frac{1}{2}}\hat{\delta}_{j+1}} + sv_{j} = 0 \quad \forall j = 0, \dots, n-1$$

$$\frac{\zeta_{j}^{\frac{1}{2}}v_{j} - \zeta_{j-1}^{\frac{1}{2}}v_{j-1}}{\hat{\zeta}_{j}^{-\frac{1}{2}}\delta_{j}} + s\hat{v}_{j} = 0 \quad \forall j = 1, \dots, n, \tag{20}$$

where the notation  $v_j = v(x_j, s)$  and  $\hat{v}_j = \hat{v}(\hat{x}_j, s)$  is used. Furthermore,  $\zeta_j$  and  $\hat{\zeta}_j$  denote averaged medium parameters at the grid locations  $x_i$  and  $\hat{x}_i$ , respectively. After symmetrization with diagonal matrices the finite-difference pencil that corresponds to (18) can be written in terms of the transpose-symmetric tridiagonal matrix

$$\begin{pmatrix}
0 & \left(\zeta_{1}\delta_{1}\hat{\zeta}_{1}^{-1}\hat{\delta}_{1}\right)^{-\frac{1}{2}} & 0 & 0 \\
\left(\zeta_{1}\delta_{1}\hat{\zeta}_{1}^{-1}\hat{\delta}_{1}\right)^{-\frac{1}{2}} & 0 & 0 \\
\vdots & -\left(\zeta_{1}\delta_{1}\hat{\zeta}_{2}^{-1}\hat{\delta}_{2}\right)^{-\frac{1}{2}} & \ddots & \ddots \\
\vdots & & \ddots & 0 & \left(\zeta_{n}\delta_{n}\hat{\zeta}_{n}^{-1}\hat{\delta}_{n}\right)^{-\frac{1}{2}} \\
0 & \cdots & 0 & \left(\zeta_{n}\delta_{n}\hat{\zeta}_{n}^{-1}\hat{\delta}_{n}\right)^{-\frac{1}{2}} & 0
\end{pmatrix}$$
(21)

In ROM embedding we try to interpret the ROM constructed from the measurement data as a discretisation of the underlying equation. If we compare the above tridiagonal discretisation stencil to the tridiagonal ROM matrix from equation (10) we find that the discretisation has twice as many unknowns as the ROM has parameters, i.e. we cannot disentangle the grid steps from the local medium parameters.

In [3] it was shown that a tridiagonal ROM that matches the lowest 2n poles and residues of the transfer function corresponds to a discretisation on a special grid, also known as the optimal grid or spectrally matched grid. This grid is independent of the medium parameter  $\zeta$  in the asymptotic limit  $n \to \infty$  and can be computed from the ROM of a reference simulation with  $\zeta_0(x) = 1$  (for details, see [3]). Let this reference grid be characterised by the primary and dual weights  $\gamma_j^0$  and  $\hat{\gamma}_j^0$ , respectively, then pointwise estimates of  $\zeta$  can be directly extracted from the ROM. To be more specific, let  $\zeta^{\rm ROM}(x)$  and  $\hat{\zeta}^{\rm ROM}(x)$  be interpolants with interpolation properties

$$\zeta^{\text{ROM}}\left(\hat{x}_{j}^{\text{optimal}}\right) = \gamma_{j}/\gamma_{j}^{0} \quad \text{where} \quad \hat{x}_{j}^{\text{optimal}} = \sum_{i=1}^{j} \hat{\gamma}_{i}^{0}$$
(22)

and

$$\hat{\zeta}^{\text{ROM}}\left(x_{j-1}^{\text{optimal}}\right) = \hat{\gamma}_{j}^{0}/\hat{\gamma}_{j} \quad \text{where} \quad x_{j}^{\text{optimal}} = \sum_{i=1}^{j} \gamma_{i}^{0},$$
 (23)

with  $x_0^{\text{optimal}} = 0$ , then it can be shown that  $\zeta^{\text{ROM}}$  and  $\hat{\zeta}^{\text{ROM}}$  converge pointwise in  $L^1(0,L)$  to the true medium profile  $\zeta$  as  $n \to \infty$ , see [3] for details.

Having discussed equation (18) using the results of [3], let us now include kinematic wave effects and consider equation (17) to obtain an optimal grid reconstruction scheme for wave propagation problems. Initially following the same procedure as above, we can show that the ratios  $\gamma_j/\gamma_j^0$  and  $\hat{\gamma}_j^0/\hat{\gamma}_j$  converge to the wave speed c[x(T)] parameterised in slowness coordinates and the optimal grids in equations (22) and (23) are primary and dual optimal slowness grids  $T_j^{\text{opt}}$  and  $\hat{T}_j^{\text{opt}}$ , respectively. To obtain the wave speed in physical coordinates, the inverse slowness transform  $x(T): T \mapsto x$  given by

$$x(T) = \int_0^T c[x(\tau)] d\tau$$
 (24)

needs to be extracted as well. This can be realized in two steps: First the optimal grid is adjusted to the average slowness of the medium and, second, the grid is locally adjusted to slowness coordinates.

The background grid should be computed for the domain [0, T(L)], however this requires knowledge of the average slowness

$$\overline{c^{-1}} = \frac{1}{L} \int_0^L c^{-1}(x) \, \mathrm{d}x \tag{25}$$

as this defines  $T(L) = L\overline{c^{-1}}$ . There are many ways to extract the average slowness from the ROM and we choose to extracted it from the first ROM coefficient  $\hat{\gamma}_1$  as

$$\overline{c^{-1}} \approx \frac{\hat{\gamma}_1 c(0)}{\hat{\gamma}_1^0},\tag{26}$$

for which obviously the wave speed c(0) at the sensor location is required. The effectiveness of the above equation is due to the fact that  $\hat{\gamma}_1^0$  depends linearly on the domain size and in the limit  $n \to \infty$  the ratio  $\frac{\hat{\gamma}_1^0 e^{-1}}{\hat{\gamma}_1}$  converges to the wave speed at x = 0. Alternatively, T(L) can be extracted from the limit  $\lim_{s\to 0} f(s)$  (see [2]).

With this in place the wave speed c(x) can be extracted from the ROM parameters as

$$\hat{c}^{\text{ROM}}\left(\hat{x}_{j}^{\text{opt}}\right) = \frac{1}{\overline{c^{-1}}} \frac{\gamma_{j}}{\gamma_{j}^{0}} \quad \forall j = 1, \dots, n$$

$$(27)$$

$$c^{\text{ROM}}\left(x_{j-1}^{\text{opt}}\right) = \overline{c^{-1}} \frac{\hat{\gamma}_{j}^{0}}{\hat{\gamma}_{j}} \quad \forall j = 1, \dots, n,$$
(28)

which are to be interpreted as pointwise estimates of the wave speed at the optimal grid points that are adjusted to the local slowness coordinates

$$x_j^{\text{opt}} = x \left( T_j^{\text{opt}} \right) = \overline{c^{-1}} \sum_{k=1}^j \gamma_k^0 \hat{c}^{\text{ROM}} \left[ x \left( \hat{T}_j^{\text{opt}} \right) \right]$$
 (29)

and

$$\hat{x}_{j}^{\text{opt}} = x \left( \hat{T}_{j}^{\text{opt}} \right) = \overline{c^{-1}} \sum_{k=1}^{j} \hat{\gamma}_{k}^{0} c^{\text{ROM}} \left[ x \left( T_{j}^{\text{opt}} \right) \right]. \tag{30}$$

These estimates converge pointwise in  $L^1(0,T(L))$  to the true wave speed which can be obtained as a corollary to theorem 6.1 in [3]. Essentially, the optimal grid embedding recovers c[x(T)] at points on the optimal grid in slowness coordinates. This recovered c[x(T)] then provides the inverse slowness transform  $T \mapsto x$ , to embed c(x) into physical space.

## 4. Krein embedding

From regular Sturm–Liouville theory it is well known that equation (1) is satisfied for infinitely many eigenpairs  $(\phi_i(x), \lambda_i)$ , with real eigenfunctions  $\phi_i(x)$  and imaginary eigenvalues  $s = \lambda_i$ . The true impedance function

$$f(s) = \sum_{i=1}^{\infty} \frac{y_i}{s + \lambda_i} + \frac{\bar{y}_i}{s + \bar{\lambda}_i}$$
(31)

is thus a meromorphic function with an infinite number of poles, corresponding to the eigenvalues  $\lambda_i$  and  $\bar{\lambda}_i$ . Now Krein and optimal grid embedding approaches both utilise truncated

spectral impedance data, and in [12] it was shown by Kac and Krein that there is a one-to-one correspondence between an n-term truncated spectral impedance function and a medium with a mass function M(x) with n points of increase. Krein embedding allows us to link this mass function to a continuous wave speed profile c(x). The following proposition provides an explicit connection between the continuous wave equation and the discrete finite-difference problem obtained from truncated spectral impedance data.

**Proposition 1 (Kac and Krein).** Let  $w_n$  satisfy the wave equation with the mass function  $M_n$ 

$$\frac{\mathrm{d}^{2}w_{n}(x,s)}{\mathrm{d}x^{2}} - s^{2}M_{n}(x)w_{n}(x,s) = 0 \quad \frac{\mathrm{d}w_{n}}{\mathrm{d}x}|_{x=0} = -s, \ w_{n}|_{x=x_{n+1}} = 0, \tag{32}$$

in the weak sense, where

$$M_n(x) = \sum_{i=0}^{n-1} \hat{\gamma}_{i+1} \delta(x - x_i), \quad x_0 = 0, \quad \text{and} \quad x_i = \sum_{k=1}^{i} \gamma_k \quad \text{for} \quad i = 1, 2, ..., n.$$
 (33)

The continuous function  $w_n$  then interpolates the finite-difference approximation from equation (6), that is, we have  $w_n(x_i) = u_i$  for i = 0, 1, ..., n.

**Proof.** The proof is straightforwardly obtained by substituting a (piecewise) linear interpolation of  $u_i$  between the  $x_i$ 's into the second-order finite-difference equation. More precisely, let  $\tilde{u}(x)$  be the linear interpolation of  $u_i$  on the grid  $\{x_i\}$ . For  $\tilde{u}(x)$  we have

$$\tilde{u}(x_i) = u_i, \tag{34}$$

$$\frac{\mathrm{d}}{\mathrm{d}x}\tilde{u}|_{x=(x_i+\delta)} = \frac{u_{i+1} - u_i}{\gamma_{i+1}}, \qquad 0 < \delta < \gamma_{i+1}$$
(35)

$$\frac{\mathrm{d}}{\mathrm{d}x}\tilde{u}|_{x=(x_i-\delta)} = \frac{u_i - u_{i-1}}{\gamma_i}, \qquad 0 < \delta < \gamma_i. \tag{36}$$

Substituting this into the second-order form of the finite-difference relation from equation (6) yields

$$\frac{\mathrm{d}}{\mathrm{d}x}\tilde{u}|_{x=(x_i+\delta)} - \frac{\mathrm{d}}{\mathrm{d}x}\tilde{u}|_{x=(x_i-\delta)} - s^2u(x_i)\hat{\gamma}_{i+1} = 0 \quad \text{for} \quad 0 < \delta < \min(\gamma_i, \gamma_{i+1})$$
 (37)

and after integration, we obtain the weak form of equation (32)

$$\int_{x_{i}-\delta}^{x_{i}+\delta} \frac{\mathrm{d}^{2}}{\mathrm{d}x^{2}} \tilde{u}(x) \, \mathrm{d}x - s^{2} \int_{x_{i}-\delta}^{x_{i}+\delta} \tilde{u}(x) \, \delta(x - x_{i}) \, \hat{\gamma}_{i+1} \mathrm{d}x = 0.$$
(38)

In Krein embedding we interpret the ROM as the impedance function at x=0 of a finite-difference discretization of the first order system (15). In particular, a two-point finite-difference discretization on a staggered grid with primary stepsizes  $\delta_j$  and dual stepsizes  $\hat{\delta}_j$  reads

$$\frac{\hat{u}_{j+1} - \hat{u}_{j}}{c_{j+1}^{-2}\hat{\delta}_{j+1}} + su_{j} = 0 \quad \forall j = 0, \dots, n-1 
\frac{u_{j} - u_{j-1}}{\delta_{j}} + s\hat{u}_{j} = 0 \quad \forall j = 1, \dots, n,$$
(39)

where we used the shorthand notation  $u_j = u(x_j, s)$  again. The primary ROM edge-weights  $\gamma_j$  are therefore interpreted as a step size  $\delta_j$  and the dual edge-weights  $\hat{\gamma}_j$  as  $c_j^{-2}\hat{\delta}_j$ . To be more precise, we introduce the nondecreasing mass function

$$M(x) = \int_{\xi=0}^{x} c^{-2}(\xi) \,d\xi \tag{40}$$

and the coordinate transform  $T \mapsto x$  given by

$$x(T) = \int_{\tau=0}^{T} c[x(\tau)] d\tau.$$
(41)

The mass function can now be written as

$$M[x(T)] = \int_{\tau=0}^{T} \frac{1}{c[x(\tau)]} d\tau$$
(42)

and we observe that

$$x_0^{\text{Krein}} = 0, \quad x_j^{\text{Krein}} = \sum_{k=1}^j \gamma_k, \quad \text{and} \quad M_n\left(x_{j-1}^{\text{Krein}}\right) = \sum_{k=1}^j \hat{\gamma}_k,$$
 (43)

for j = 1, 2, ..., n can be interpreted as ROM quadrature rules of (41) and (42), respectively. Finally, if we let  $T_j^{\text{Krein}}$  denote the slowness coordinate corresponding to  $x_j^{\text{Krein}}$  then, using the results of the optimal grid case discussed in the previous section, we have

$$\chi_n \left[ T_j^{\text{Krein}} \right] = x_j^{\text{Krein}} = \sum_{k=1}^j \gamma_k = \overline{c^{-1}} \sum_{k=1}^j c^{\text{ROM}} \left( \hat{x}_k^{\text{opt}} \right) \gamma_k^0 \tag{44}$$

and

$$M_n \left[ \chi_n \left( T_{j-1}^{\text{Krein}} \right) \right] = \sum_{k=1}^j \hat{\gamma}_k = \overline{c^{-1}} \sum_{k=1}^j c^{\text{ROM}} \left( x_{k-1}^{opt} \right)^{-1} \hat{\gamma}_k^0.$$
 (45)

Convergence of the Krein embedding follows directly from equations (44) and (45). Since the optimal grid parameters converge, convergence of  $\chi_n(T) \mapsto x(T)$  and  $M_n(x) \mapsto M(x)$  follows again as a corollary of theorem 6.1 in [3].

#### 5. Numerical examples

Optimal grid embedding leads to pointwise estimates for the wave speed c(x), whereas Krein embedding leads to an estimation of the mass function  $M(x) = \int_0^x c^{-2}(\xi) d\xi$ . Therefore, it is natural to display the inversion result of the optimal grid embedding and Krein embedding in terms of these two quantities.

In figure 2 the dashed line signifies a smoothly varying velocity profile on the interval [0,2] that we attempt to reconstruct using knowledge of poles and residues of the impedance function at x = 0. This spectral data is obtained by applying the vectorfit algorithm [8] to the impedance function at x = 0 to obtain a rational function representation in pole-residue form as indicated in equation (2).

We start with n = 12 pole-residue pairs of the impedance function f(s) to construct a ROM and realise optimal grid and Krein embeddings. In this example, the background grid in case of optimal grid embedding is extracted from a reference simulation with a constant  $c_0 = 1$ . With only n = 12 spectral points, the wave speed c(x) in case of an optimal grid embedding and the mass function M(x) in case of Krein embedding are accurately reconstructed as illustrated in

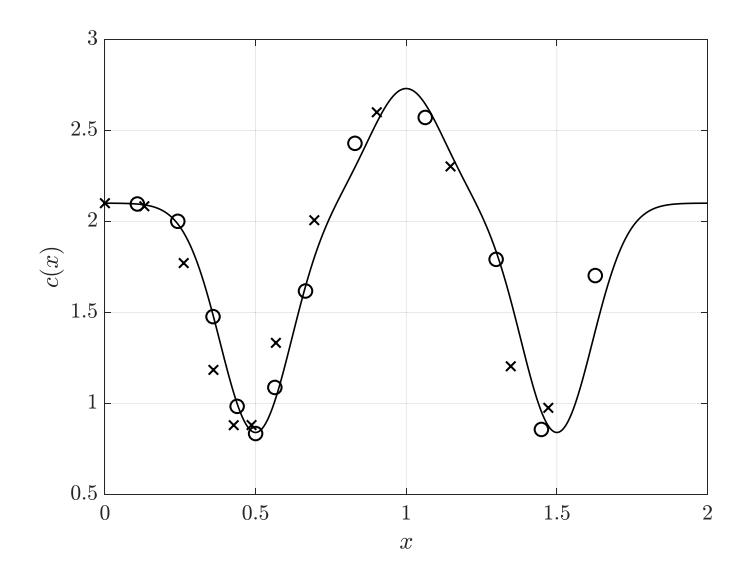


**Figure 2.** Velocity profile c(x) (solid line) and optimal grid reconstruction of this profile based on n = 12 pole-residue pairs of the impedance function at x = 0. Crosses: reconstructed velocity values at primary nodes. Circles: reconstructed velocity values at dual nodes.

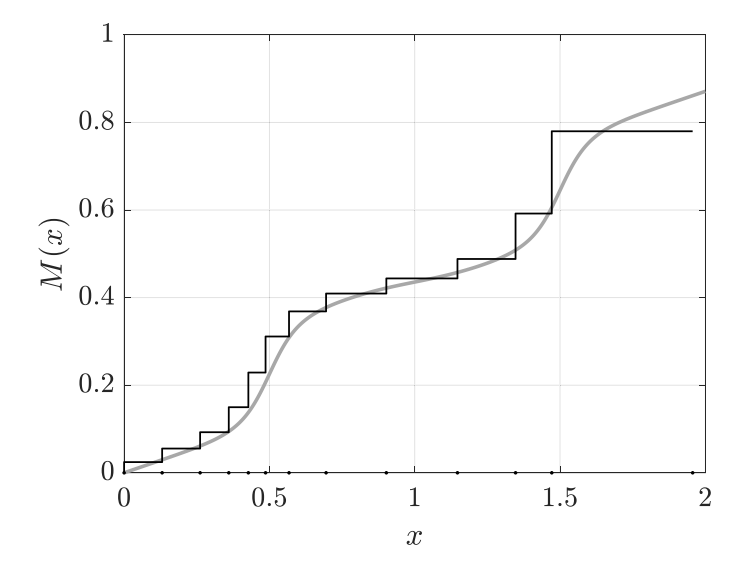


**Figure 3.** Mass function M(x) (solid grey line) and Krein embedding reconstruction of this function (solid black line) based on n = 12 pole-residue pairs of the impedance function at x = 0. The Krein grid is visualized with small dots on the x-axis.

figures 2 and 3, respectively. We note that due to the low number of pole-residue pairs that are used, the estimates are slightly misplaced as the map  $T \mapsto x$  is estimated with only a few quadrature points.

Therefore, let us increase the number of pole-residue pairs to n = 50. In this case we show the performance of optimal grid and Krein embedding in terms of velocity profile and mass

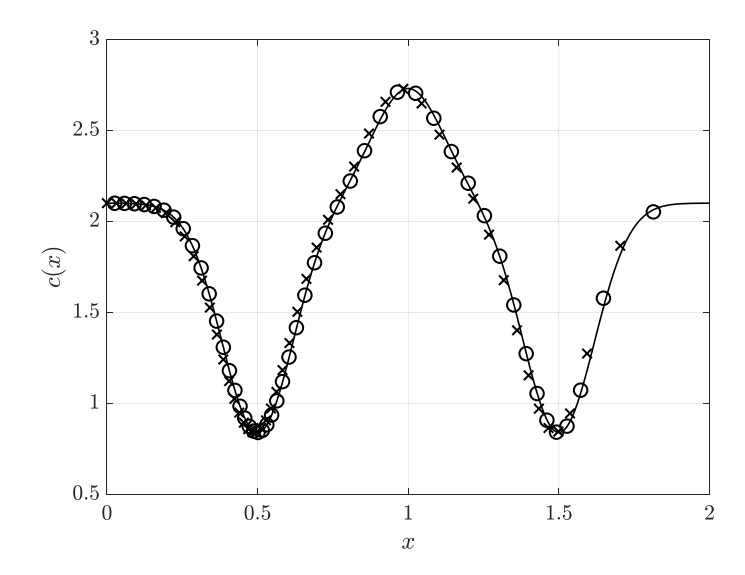


**Figure 4.** Optimal grid embedding reconstruction of the velocity profile (solid line) based on n = 50 pole-residue pairs of the impedance function at x = 0. Crosses: reconstructed velocity values at primary nodes, circles: reconstructed velocity values at dual nodes.

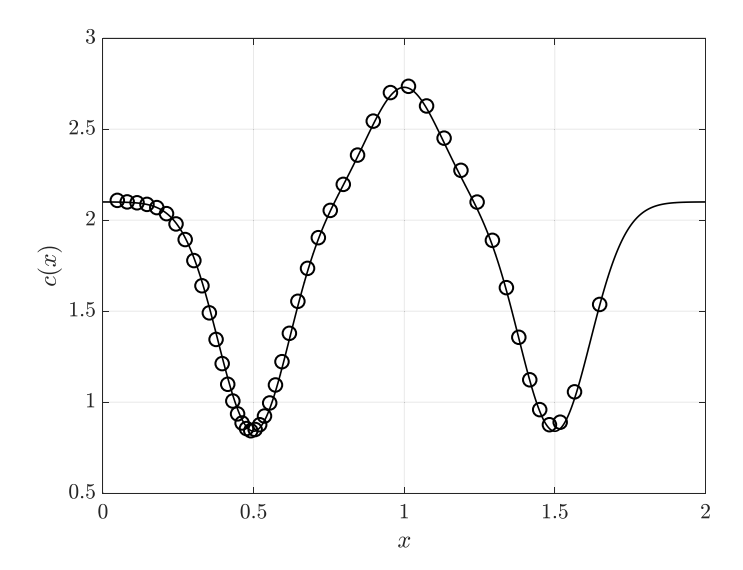


**Figure 5.** Krein embedding reconstruction (circles) of the velocity profile (solid line) based on n = 50 pole-residue pairs of the impedance function at x = 0.

function reconstruction. Figure 4 shows the optimal grid embedding reconstruction for n = 50, and clearly indicates convergence of the optimal grid embedding approach. Figure 5 shows the velocity profile reconstruction with the Krein embedding approach, which indicates that Krein embedding converges as well. Finally, mass function reconstructions for optimal grid and Krein embedding are shown in figures 6 and 7, respectively. These reconstruction results

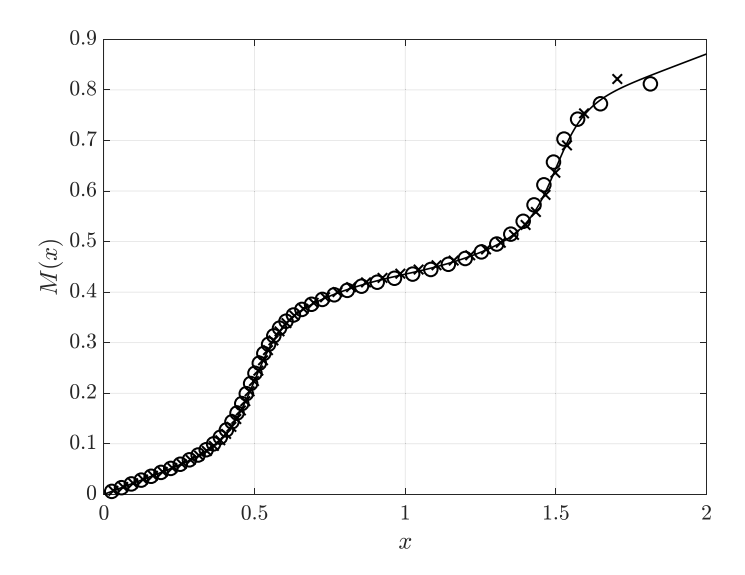


**Figure 6.** Optimal grid embedding reconstruction of the mass function (solid line) based on n = 50 pole-residue pairs of the impedance function at x = 0. Crosses: reconstructed mass function values at primary nodes, circles: reconstructed mass function values at dual nodes.

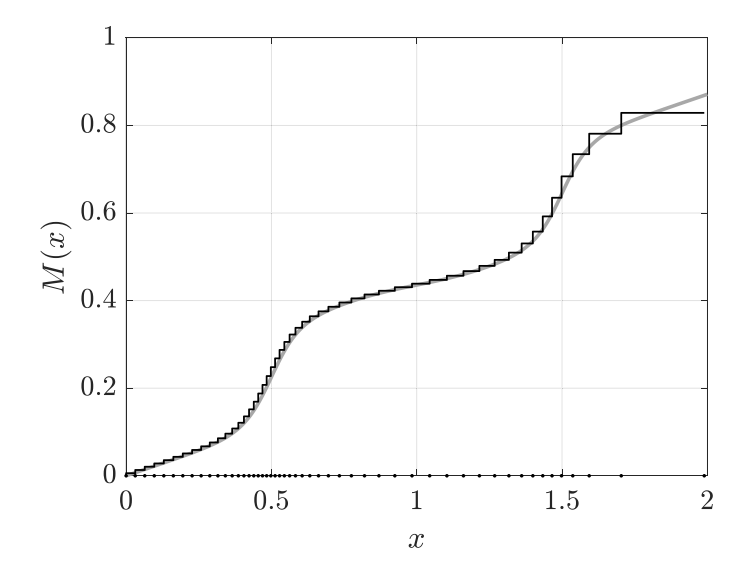


**Figure 7.** Krein embedding reconstruction (black line) of the mass function (grey line) based on n = 50 pole-residue pairs of the impedance function at x = 0. The nodes of the Krein grid are shown as solid dots on the x-axis.

indicate that both embedding approaches converge and benefit if more spectral data (pole-residue pairs) of the impedance function is available.

Finally, we show how the two embedding approaches reconstruct a smoothed step (piecewise constant) velocity profile. The dashed line in figure 8 shows the velocity profile along with the optimal grid embedding reconstruction for n = 50. Clearly, optimal grid embedding

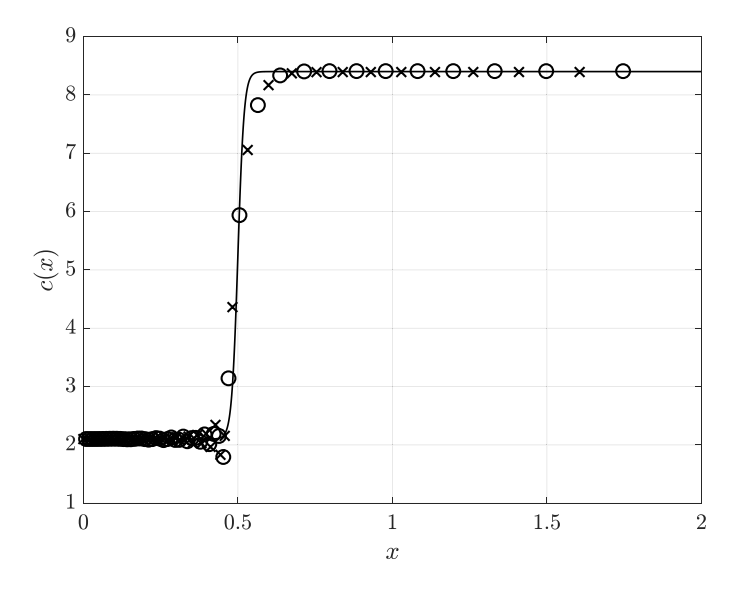


**Figure 8.** Optimal grid embedding reconstruction of a step velocity profile (solid line) based on n = 50 pole-residue pairs of the impedance function at x = 0. Crosses: reconstructed velocity values at primary nodes, circles: reconstructed velocity values at dual nodes.

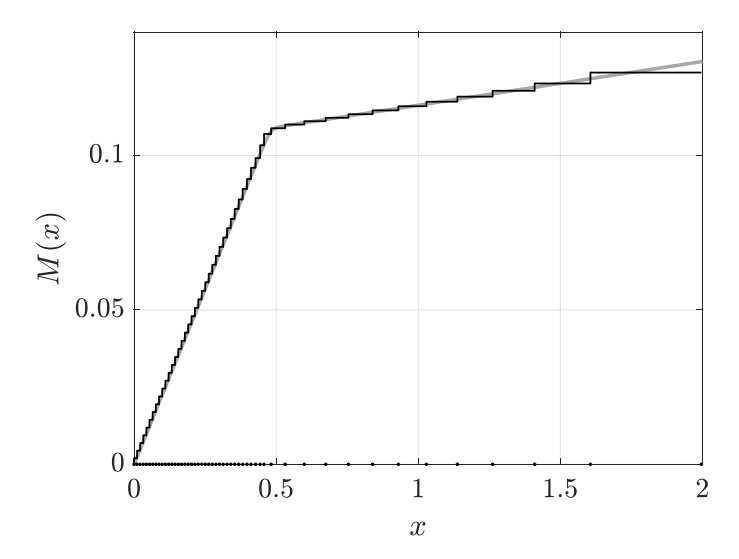


**Figure 9.** Krein embedding reconstruction (black line) of the mass function (grey line) based on n = 50 pole-residue pairs of the impedance function at x = 0. The nodes of the Krein grid are shown as solid dots on the x-axis.

captures the exact wave speed away from the step and shows some Gibbs ringing around the step. The Krein embedding reconstruction for n = 50 of the corresponding mass function is shown in figure 9. Here Gibbs ringing is not observed, since M(x) is an increasing quantity. For this example the effects of noisy data on the reconstruction is shown in appendix C.



**Figure 10.** Illustration of primary (crosses) and dual (circles) grid nodes of an optimal/Krein grid for a semi-infinite-domain. The grid steps become progressively large as we move away from the measurement point, which coincides with the left-most primary grid node.

#### 6. Embedding of ROMs on semi-infinite domains

Up till now, we have considered scattering problems on bounded domains. For semi-infinite domains, that is, domains that extend to infinity in one direction, the optimal and Krein grids may be applied, but these approaches produce excessively large step sizes [10] as illustrated in figure 10.

This problem can be avoided, however, by constructing ROMs that can be interpreted as two-point finite-difference discretisations of dissipative first-order continuous wave equations. We refer to this approach as *Krein-Nudelman embedding* [13].

To be specific, consider the wave equation in the Laplace domain on a semi-infinite domain, where the wave speed variations are supported on (0,L) and the wave speed is constant c(x) = c(L) for all x > L

$$\frac{d^{2}u(x,s)}{dx^{2}} - s^{2} \frac{1}{c^{2}(x)} u(x,s) = 0, \quad \frac{du}{dx}\Big|_{x=0} = -s, \quad \text{and} \quad \lim_{x \to L} \frac{du}{dx} = \frac{-s}{c(L)} u(L,s). \tag{46}$$

The boundary condition at x = L is the Sommerfeld radiation condition only satisfied by waves traveling in the positive x-direction ( $\exp[-sx/c(L)]$ ). We note that the Sommerfeld condition can be enforced at an arbitrary point x > L since all waves beyond this point travel in the positive x direction. The inverse problem is the recovery of  $M(x) = \int_0^x c(\xi)^{-2} d\xi$  from impedance measurements f(s) = u(0,s).

The impedance function measured at x = 0 for an open domain does not have a point spectrum. To implement Krein–Nudelman embedding, we fit the impedance function with rational functions with n complex-conjugate pole-residue pairs. Since the impedance function is passive, the poles and residues have a positive real part. In the presented results, we use vector fit [8] to obtain the poles and residues from the impedance function.

With complex poles and residues the diagonal entries (called  $\alpha$  in algorithm 1) of the tridiagonal matrix obtained from the Lanczos algorithm are no longer zero. Since similar matrices have the same trace we can equate the sum of the eigenvalues in  $\Lambda$  to the sum of the diagonal elements of  $\mathbf{T}^{TS}$ , called  $\alpha_i$ 's in the Lanczos algorithm

$$0 < \operatorname{trace}(\mathbf{\Lambda}) = \operatorname{trace}(\mathbf{T}^{\mathrm{TS}}) = \sum_{i=1}^{n} \lambda_i + \overline{\lambda_i} = \sum_{i=1}^{2n} \alpha_i$$
 (47)

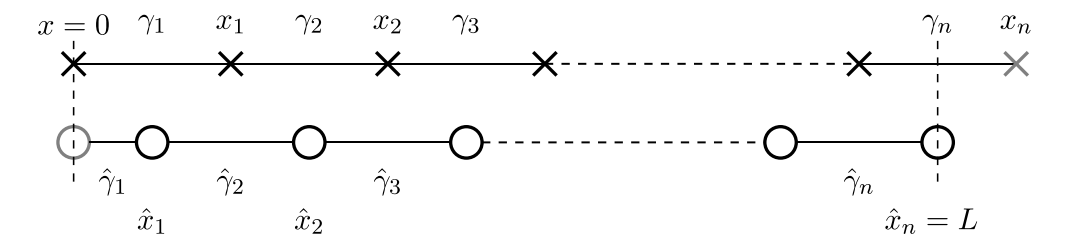


**Figure 11.** Grid used to interpret the ROM as a finite-difference discretisation of the underlying differential operator on a semi-infinite domain. The crosses represent primary grid nodes and the circles dual grid nodes. Note that the open boundary condition is applied at the last dual node x = L.

and see that the diagonal entries cannot all vanish. These diagonal elements are interpreted as a loss term in Krein-Nudelman embedding and absorb energy. To facilitate an embedding that allows for absorption, we introduce the complex symmetry tridiagonal matrix  $T^{TS;open}$ 

$$\mathbf{T}^{\text{TS;open}} = \begin{pmatrix} \alpha_{1} & -i(\gamma_{1}\hat{\gamma}_{1})^{-\frac{1}{2}} & 0 & & 0 \\ -i(\gamma_{1}\hat{\gamma}_{1})^{-\frac{1}{2}} & \alpha_{2} & i(\gamma_{1}\hat{\gamma}_{2})^{-\frac{1}{2}} & 0 & & \\ \vdots & i(\gamma_{1}\hat{\gamma}_{2})^{-\frac{1}{2}} & \ddots & \ddots & & \\ \vdots & & \ddots & & \alpha_{2n-1} & -i(\gamma_{n}\hat{\gamma}_{n})^{-\frac{1}{2}} \\ 0 & \cdots & 0 & -i(\gamma_{n}\hat{\gamma}_{n})^{-\frac{1}{2}} & \alpha_{2n} \end{pmatrix}, \tag{48}$$

which we obtain from running the Lanczos algorithm with the complex poles and residues obtained from fitting the impedance function of a semi-infinite domain.

To interpret this tridiagonal matrix using Krein-Nudelman embedding consider a finite-difference discretization of equation (46) on the grid displayed in figure 11

$$\frac{\hat{u}_{j+1} - \hat{u}_{j}}{c_{j+1}^{-2}\hat{\delta}_{j+1}} + su_{j} = 0 \quad \forall j = 0, \dots, n-1 
\frac{u_{j} - u_{j-1}}{\delta_{j}} + s\hat{u}_{j} = 0 \quad \forall j = 1, \dots, n-1, 
-u_{n} + c(L)\hat{u}_{n} + s\frac{1}{2}\delta_{n}\hat{u}_{j} = 0$$
(49)

and compare it to finite difference discretization introduced by the tridiagonal matrix in equation (48)

$$\frac{\hat{u}_{j+1} - \hat{u}_j}{\hat{\gamma}_{j+1}} + (\alpha_{2j+1} + s) u_j = 0, \qquad \forall j = 0, \dots, n-1, 
\frac{u_j - u_{j-1}}{\gamma_j} + (\alpha_{2j} + s) \hat{u}_j = 0, \qquad \forall j = 1, \dots, n.$$
(50)

Note that the Sommerfeld condition is applied on the last dual grid point, whereas the Dirichlet condition in the bounded domain was applied on the last primary grid node.

The diagonal of  $T^{TS;open}$  appears as a loss terms in the equation, and can thus be used to define integrated primary and dual loss coefficients

$$r_i = \hat{\gamma}_i \, \alpha_{2i-1} \quad \text{and} \quad \hat{r}_i = \gamma_i \, \alpha_{2i}.$$
 (51)

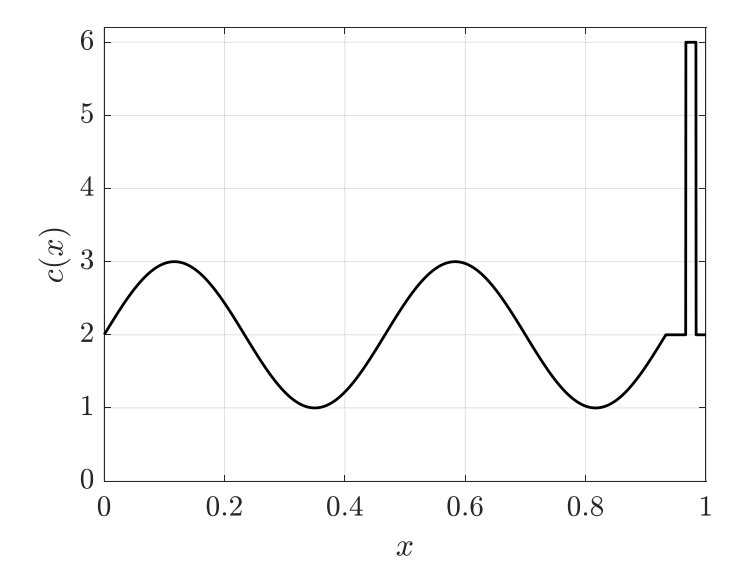


**Figure 12.** Wave speed model for the semi-infinite domain example. A reflector is placed at the end of the medium.

A Sommerfeld radiation condition would be equivalent to all  $r_i$  and  $\hat{r}_i$  values vanishing except for  $\hat{r}_n$ .

To illustrate this embedding we consider the inverse problem of recovering the velocity profile in figure 12 from impedance measurements at x = 0. We use n = 121 pole-residue pairs to fit the impedance function and compute  $\mathbf{T}^{\text{TS;open}}$  using the complex symmetric Lanczos algorithm. Further numerical details can be found in appendix  $\mathbf{B}$ .

The Krein-Nudelman embedding of the obtained mass function is shown alongside the true mass function in figure 13. The smooth velocity variations are recovered well, whereas the reflector is not recovered.

In figure 14 the loss coefficients are embedded into space for visualisation purposes. The primary losses are displayed on the Krein grid and the dual losses in between Krein grid nodes. Almost all losses  $r/\hat{r}$  vanish up until the last reflector in the medium, where the last  $\hat{r}_i$  contribute to an effective loss term. The recovered r and  $\hat{r}$  terms do not exactly correspond to a Sommerfeld radiation condition, but rather an effective absorbing medium being placed at the end of the Krein embedding. Nonetheless, the velocity profile up to the last reflector is well recovered at which point the loss coefficients increase. Note that the last grid point of the Krein embedding is outside the interval of wave speed variations, since the Sommerfeld condition is prescribed on a dual grid node in between the Krein-grid nodes.

Here we reach a fundamental limitation of the Krein embedding. From the fitted pole residue form, the Krein embedding cannot distinguish between an infinite lossless medium, which does not have a point spectrum, and a finite-absorbing medium. See the appendix A for a further discussion.

However, up until the Krein embedding recovers an 'effective' absorbing medium the embedding can be used to solve inverse problems. This is in some sense physical as one typically does not know from which point the infinite domain has constant medium parameters. Compared to an optimal grid approach, the Krein-Nudelman approach only produces a grid

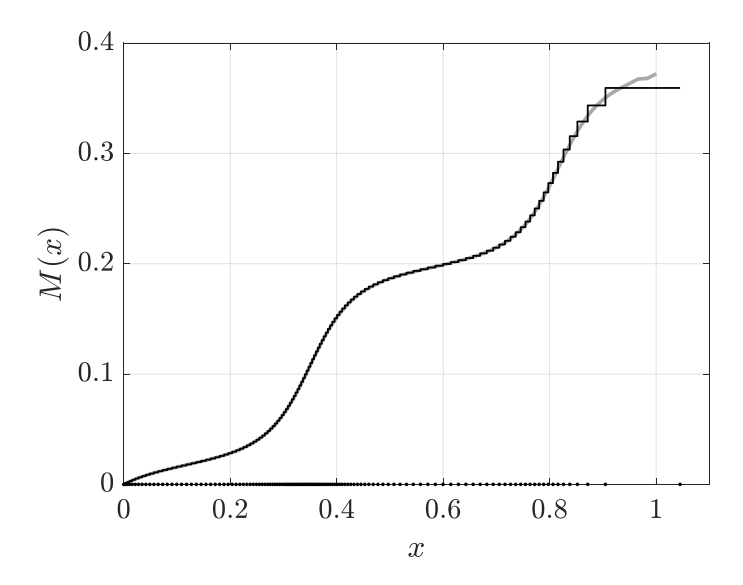


**Figure 13.** Mass function M(x) (solid black line) and Krein embedding grid reconstruction of this function (grey solid line) based on n = 121 pole-residue pairs approximating the impedance function at x = 0.

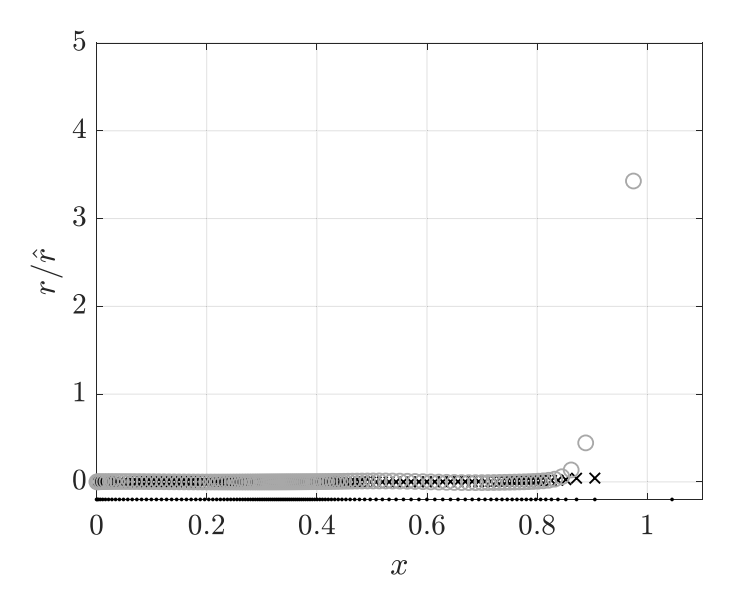


**Figure 14.** Embedding: primary  $r_i$  (×) losses embedded on the Krein grid  $\chi^{\text{Krein}}$  and dual losses  $\hat{r}_i$  ( $\circ$ ) embedded centred between Krein grid nodes. An effective absorbing inclusion is placed at the end of the domain by the Krein embedding.

in the interval where the variations of the wave speed are supported, whereas the optimal grid approach places grid points beyond the variations of the medium, which is not useful for inversion.

#### 7. Conclusions

In this paper, we discussed two so-called ROM embedding procedures to solve inverse scattering problems based on spectral impedance data collected at one end of an interval of interest. More precisely, we have shown that starting from impedance data in pole-residue form, the Lanczos algorithm can be used to construct ROMs that can be interpreted as two-point finite-difference discretisations of first-order wave equations. We call this ROM embedding and presented two such embedding procedures, namely, optimal grid and Krein embedding.

The optimal grid embedding procedure is based on the theory of optimal grids and was implemented in terms of spatial coordinates instead of travel time coordinates. In this approach, the wave speed profile of an inhomogeneous medium can be reconstructed if we first determine an optimal reference grid for a (homogeneous) reference medium. The use of a reference grid is avoided, however, in the Krein embedding approach, and convergence results obtained for optimal grid embedding can be used to demonstrate the convergence of Krein embedding as well. Furthermore, since no reference grid is necessary for Krein embedding, it may be possible to apply this procedure to semi-infinite domains. Here we run into uniqueness problems, however, since with an impedance function in pole-residue form, it is impossible to distinguish between a lossy medium on a bounded interval and a lossless medium on a semi-infinite interval. Nevertheless, numerical examples indicate that the wave speed profile is reconstructed on a semi-infinite domain up till the last reflector that is present within this domain. Future work will focus on the development of a ROM embedding procedure for semi-infinite domain problems.

## Data availability statement

All data that support the findings of this study are included within the article (and any supplementary files).

## **Acknowledgments**

We thank Liliana Borcea, Alex Mamonov, and Mikhail Zaslavsky for many stimulating discussions. The work of Vladimir Druskin was financially supported by AFOSR Grants FA 955020-1-0079 and FA9550-23-1-0220, and NSF Grant DMS-2110773. The work of Elena Cherkaev was financially supported by NSF Grant DMS-2111117. The work of Murthy Guddati was financially supported by NSF Grant DMS-2111234. The work of Jörn Zimmerling was financially supported by NSF Grant DMS-2110265. This support is gratefully acknowledged.

# Appendix A. Can one distinguish bounded-lossy inverse problems from unbounded-open inverse problems based on Stieltjes functions?

Consider the system  $Au = \lambda u + g$ , where A is a Hermitian nonnegative operator, and u and g are elements belonging to a Hilbert space. We introduce the transfer function of this system as  $f(\lambda) = g^*u$ , where the asterisk denotes the Hermitian inner product on the Hilbert space. This transfer function is a Stieltjes function. Recall that a function  $f(\lambda)$  is a Stieltjes function if

$$f(\lambda) = \int_{z=-\infty}^{0} \frac{\rho(z)}{\lambda - z} dz, \quad \lambda \in \mathbb{C} \setminus \mathbb{R}_{-},$$
(A1)

for some positive distribution  $\rho(z)$  defined as the generalised derivative of a probability measure.

Subsequently, we consider the first-order system

$$\left(\begin{array}{cc} -\sigma & L \\ L^* & 0 \end{array}\right) \left(\begin{array}{c} \tilde{u} \\ v \end{array}\right) = s \left(\begin{array}{c} \tilde{u} \\ v \end{array}\right) + \left(\begin{array}{c} g \\ 0 \end{array}\right),$$

on a Hilbert space, where  $L^*$  is the adjoint of operator L and  $\sigma \geqslant 0$ . The transfer function of this system is introduced as  $h(s) = g^* \tilde{u}$ . A lossless first-order system is characterised by  $\sigma = 0$  everywhere, while if  $\sigma > 0$  in some domain in space, we refer to the above system as a lossy first-order system.

Eliminating v in the lossless case, we obtain the Hermitian system  $A\tilde{u} = \lambda \tilde{u} + sg$  with  $A = LL^*$  and  $\lambda = s^2$ . Here, the transfer functions of the Hermitian and first-order system are related by  $f(\lambda) = \lambda^{-1/2}h(\lambda^{1/2})$  and h satisfies the three criteria for a passive SISO system, that is, we have

- (i) h(s) has no poles in  $\mathbb{C}_+$ ,
- (ii)  $h(\bar{s}) = \bar{h}(s)$  for every  $s \in \mathbb{C}_+$ , where the overbar denotes complex conjugation, and
- (iii)  $\operatorname{Re}[h(i\omega+0)] \geqslant 0$  for  $\omega \in \mathbb{R}$ .

For a lossy first-order system, the transfer function h(s) still satisfies the above three criteria, but we no longer arrive at a Hermitian form when v is eliminated from the first-order system. However, we can establish an isomorphism between passive transfer functions and Stieltjes functions. More precisely, we have

**Proposition 2.** Using  $f(\lambda) = \lambda^{-1/2}h(\lambda^{1/2})$ , every Stieltjes function  $f(\lambda)$  can be transformed to a passive transfer function  $h(\lambda^{1/2})$  and vice versa.

**Proof.** Consider the transformation  $f \to h$ . First note that from the definition (A1) of a Stieltjes function it follows that  $f(\lambda)$  is an analytic function of  $\lambda$  on  $\mathbb{C} \setminus \mathbb{R}_-$ . Setting  $s = \lambda^{1/2}$ , it follows from  $h(s) = sf(s^2)$  and the analyticity of f that h(s) is analytic in  $\mathbb{C}_+$  and therefore h(s) has no poles in  $\mathbb{C}_+$ . Furthermore, since  $\rho$  is real (positive), we have  $\bar{f}(s^2) = f(\bar{s}^2)$  and it follows that  $\bar{h}(s) = h(\bar{s})$  with  $s \in \mathbb{C}_+$ . Finally, we have

$$\lim_{\epsilon \downarrow 0} \operatorname{Re}\left[h(\epsilon + \mathrm{i}\omega)\right] = \lim_{\epsilon \downarrow 0} \frac{1}{2} \left[h(\epsilon + \mathrm{i}\omega) + h(\epsilon - \mathrm{i}\omega)\right] = \pi \left|\omega\right| \rho\left(-\omega^2\right) > 0, \quad (A2)$$

where we have used  $h(s) = sf(s^2)$  and

$$\rho(\lambda) = \frac{f(\lambda + i0) - f(\lambda - i0)}{2\pi i}, \text{ with } \lambda \in \mathbb{R}_{-}.$$

Reasoning in reverse order gives the 'vice versa' result.

Now to each Stieltjes function there corresponds a unique Stieltjes–Krein string [12] and a consequence of the above proposition is that we cannot distinguish between lossy media and lossless media on a semi-infinite domain, since in both cases the transfer function is passive.

# Appendix B. Details on the numerical implementation of the open domain problem

For the Krein–Nudelman embedding on an open domain, we need to extract a rational function from the measured impedance data. There are many rational fitting methods available, and in this work we used the vectorfit algorithm [8].

In the open domain problem considered in the main text, we evaluate the impedance on the interval  $s \in i[-\omega_{\max}, \omega_{\max}]$ , discretized at 3000 equidistant points, and then use the vectorfit algorithm to extract the poles and residues. The number of poles and residues n depends on  $\omega_{\max}$  and in the presented experiment we increase n iteratively until the relative error of the fit reaches  $10^{-11}$ . The initial poles of the vectorfit algorithm were chosen equidistantly in the frequency interval of interest  $i[-\omega_{\max},\omega_{\max}]$  with a small real shift chosen as  $0.01\omega_{\max}$ . After three iterations of the vectorfit algorithm, we obtained the desired misfit. In our example, we choose  $\omega_{\max}$  such that it corresponds to a wavelength of 1/50 in a constant background medium of c(x) = 2 on the interval  $x \in [0, 1]$ .

Using standard vectorfit, we have obtained passive pole residue forms in all experiments and the recovery of the spectral data is stable with respect to changes in the initial poles. Alternatively, fitting methods that enforce passivity could be used (see [1, 6, 7, 9], for example).

The degree n of the rational function that can be fitted to the impedance data determines the number of points of increase of the Krein embedding M(x). In one spatial dimension this number is roughly proportional to the length of the frequency interval. Further, each residue/pole pair needs to significantly contribute to the data and should be deflated otherwise. In practice, the Hankel-singular values of the resulting ROM should be above noise level/machine precision. Overfitting will lead to a breakdown of the method as the passivity of the step sizes in Krein embedding cannot be guaranteed in that case.

#### Appendix C. Robustness of Krein embedding

To show the robustness of the Krein embedding approach with respect to noise, we perturb the residues and eigenvalues and compute the Krein embedding and optimal grid embedding. Specifically, we add 5% i.i.d. Gaussian noise to the gaps of the eigenvalues  $\lambda_j$  and 5% i.i.d. Gaussian noise to the square root of the residues  $\sqrt{y_j}$  and compute the optimal grid and Krein embedding for the step velocity profile considered in the main text. In figure C1 the optimal grid embedding is shown for 50 pole residue pairs and in figure C2 the Krein embedding is shown.

We observe that both embedding methods capture the jump in the velocity profile and the reconstruction is less accurate than in the noiseless case. We stress that no regularization is used in both embedding approaches.

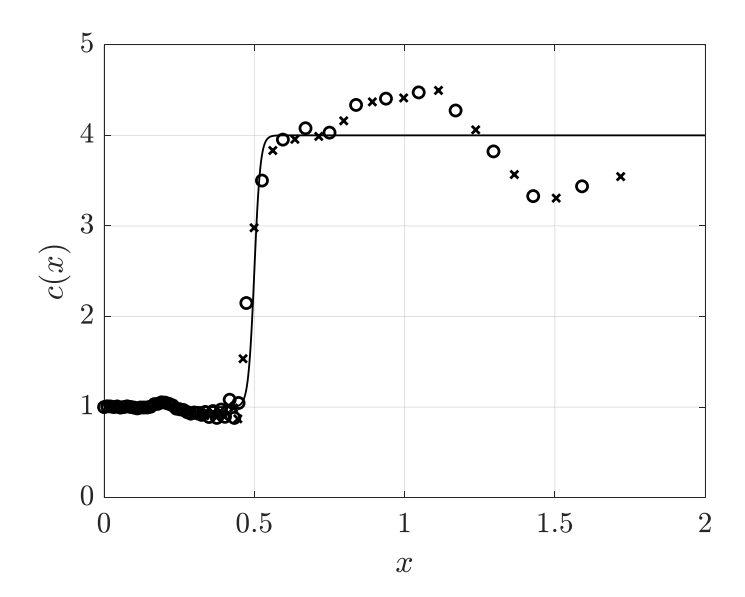


**Figure C1.** Velocity profile c(x) (solid line) and optimal grid reconstruction of this step profile based on n = 50 noisy pole-residue pairs of the impedance function at x = 0. Crosses: reconstructed velocity values at primary nodes. Circles: reconstructed velocity values at dual nodes.

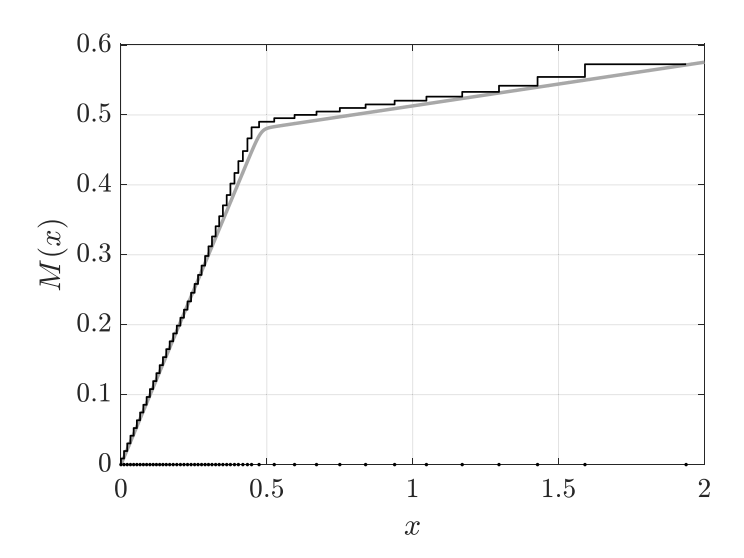


**Figure C2.** Mass function M(x) (solid grey line) and Krein embedding reconstruction of this function (solid black line) based on n = 50 noisy pole-residue pairs of the impedance function at x = 0. The Krein grid is visualized with small dots on the x-axis.

## **ORCID iD**

Rob Remis https://orcid.org/0000-0003-0365-4942

#### References

- Benner P, Goyal P and Van Dooren P 2020 Identification of port-Hamiltonian systems from frequency response data Syst. Control Lett. 143 104741
- [2] Borcea L and Druskin V 2002 Optimal finite difference grids for direct and inverse Sturm-Liouville problems *Inverse Problems* 18 979–1001
- [3] Borcea L, Druskin V and Knizhnerman L 2005 On the continuum limit of a discrete inverse spectral problem on optimal finite difference grids Commun. Pure Appl. Math. 58 1231–79
- [4] Borcea L, Druskin V and Zimmerling J 2021 A reduced order model approach to inverse scattering in lossy layered media J. Sci. Comput. 89 1–36
- [5] Collin R E 1991 Field Theory of Guided Waves 2nd edn (IEEE-Press)
- [6] Deschrijver D and Dhaene T 2004 Passivity-based sample selection and adaptive vector fitting algorithm for pole-residue modeling of sparse frequency-domain data *Proc. 2004 IEEE Int. Behavioral Modeling and Simulation Conf. (BMAS) (San Jose, CA)* pp 68–73
- [7] Grivet-Talocia S 2007 An adaptive sampling technique for passivity characterization and enforcement of large interconnect macromodels *IEEE Trans. Adv. Packag.* 30 226–37
- [8] Gustavsen B and Semlyen A 1999 Rational approximation of frequency domain responses by vector fitting IEEE Trans. Power Deliv. 14 1052–61
- [9] Gustavsen B and Semlyen A 2001 Enforcing passivity for admittance matrices approximated by rational functions *IEEE Trans. Power Syst.* 16 97–104
- [10] Ingerman D, Druskin V and Knizhnerman L 2000 Optimal finite difference grids and rational approximations of the square root I. Elliptic problems Commun. Pure Appl. Math. 53 1039–66
- [11] Jaulent M 1982 The inverse scattering problem for *LCRG* transmission lines *J. Math. Phys.* 23 2286–90
- [12] Kac I S and Krein M G 1974 On the spectral functions of the string *Am. Math. Soc. Transl.* **103** 19–102 (Engl. transl.)
- [13] Krein M G and Nudelman A A 1989 Some spectral properties of a nonhomogeneous string with a dissipative boundary condition J. Oper. Theory 22 369–95 (in Russian)
- [14] Marshall T 1969 Synthesis of RLC ladder networks by matrix tridiagonalization IEEE Trans. Circuit Theory 16 39–46
- [15] Natterer F 1998 A discrete Gelfand-Levitan theory *Technical Report* (Institut für Numerische und instrumentelle Mathematik Universitaet Muenster Germany) (available on the author's website)
- [16] Saad Y 1982 The Lanczos biorthogonalization algorithm and other oblique projection methods for solving large unsymmetric systems SIAM J. Numer. Anal. 19 485–506
- [17] Sjostrand J and Zworski M 1991 Complex scaling and the distribution of scattering poles J. Am. Math. Soc. 4 729–69
- [18] Virieux J and Operto S 2009 An overview of full-waveform inversion in exploration geophysics Geophysics 74 WCC1–26